AIAA JOURNAL
Vol. 34, No. 5, May 1996

Flow over an Obstacle Emerging from the Wall of a Channel

Henry A. Carlson* and John L. Lumley†
Cornell University, Ithaca, New York 14850

Direct simulation of laminar flow over a rising obstacle (an actuator) reveals the presence of vortical structures identical to those found in flow over a stationary obstacle, intensified and stretched by the upward velocity of the boundary. Following deceleration of the actuator to a stationary position, this amplification leads to a vortex shedding event in the wake region as the flow evolves toward its steady state. Three obstacle shapes are analyzed: one is streamwise symmetric, and two are skew symmetric. The symmetric actuator is also raised into a higher Reynolds number flow and in a final test is raised at half-speed into the low Reynolds number flow. Results indicate that the time scale of the transient is independent of Reynolds number, depending primarily upon the rising time of the actuator and to a lesser degree its shape.

I. Introduction

ACTIVE control in the turbulent boundary layer of a wall-bounded flow is an area of research that has significant implications for the air transport industry: substantial reductions in fuel costs may be achieved through small reductions in skin-friction drag; higher operating temperatures (and better efficiency) may be obtained in gas turbines through control of the heat transfer between exhaust gases from the combustor and the turbine blades. Different strategies for control include mass transfer through porous walls[1] and so-called smart skins: an actuator on the wall responds to a flow by adjusting its height to steer the wall region dynamics (the bursting processes that are signatures of turbulent flows and primary sources of momentum and heat transport).[2]

Critical to the success of active control is not only an understanding of near-wall turbulence (a great deal of research has been directed toward this over the past 30 years) but also an understanding of the phenomena that are to be used to effect control—the transient behavior of flow over a moving obstacle (concerning which little data are available). Flows over three-dimensional, stationary obstacles have been studied in the laboratory, in the physical domain, and through numerical simulation.[3–6] In a comprehensive survey consisting of both experimental and computational tests, Mason and Morton[7] have analyzed laminar, steady flows past a variety of stationary obstacles.

As an extension of this body of work, focus is redirected toward transients associated with obstacles that emerge in time, utilizing an algorithm that simulates flow in a channel with three-dimensional, time-dependent wall geometries. The code has been verified using wall geometries for which there exist known steady and unsteady solutions[8]; this includes comparisons with data from Mason and Morton.[7] Between these benchmark tests involving simpler flows and the control work involving turbulent flows fall intermediate analyses of transients associated with low and moderate Reynolds number laminar flows over rapidly emerging obstacles.

To distinguish between the stationary and the rising obstacle, the latter shall be referred to as an actuator. Three actuator shapes have been selected, one streamwise symmetric and two skew symmetric. All are smooth functions, symmetric in the spanwise (crossflow) direction. As in the cases analyzed by Mason and Morton,[7] Reynolds numbers have been chosen that lie below the value at which flow (over a stationary obstacle) becomes unsteady.

Using a local Reynolds number (Re_l), based on obstacle height and the mean velocity that would exist through the height interval in the absence of the obstacle, Mason and Morton[7] report that this transitional value is approximately 1.60×10^2. The high Reynolds number, unsteady wake behind a stationary obstacle must be distinguished from the subject of this investigation: low and moderate Reynolds number flows over a rapidly emerging obstacle, unsteady in the short term, steady in the long term.

Here, the selected local Reynolds numbers are 2.88×10^1 and 7.2×10^1. Based upon outer variables (channel half-height and mean velocity at the channel centerline) the Reynolds numbers (Re) are 2×10^3 and 5×10^3. Values have been chosen that produce different short-term transients: a stagnation zone upstream at the lower number and separated flow upstream at the higher (each with a separation region downstream). With the given computational domain and spatial resolution $Re = 5 \times 10^3$ marks the threshold above which solutions become underresolved, exhibiting characteristic roughness.

The numerical method, described in Sec. II, consists of a spectral representation of the solution. Periodic boundary conditions in the streamwise direction preclude explicit prescription of in- and outflow conditions. These are specified implicitly through the addition of a damping term, Gaussian in the streamwise direction with peak values at the inlet and outlet of the computational box.[9] With the inclusion of this term, flow approaching the actuator is parabolic and steady (Poiseuille flow).

The damping zones prevent outflow disturbances from re-entering the box, providing a clear picture of the flow dynamics adjacent to a solitary, emerging obstacle. The simulations reveal the presence of vortical structures identical to those found in flow over a stationary obstacle, intensified and stretched by the upward velocity of the boundary. Following deceleration of an actuator to a stationary position, this amplification leads to a transient, common in all test cases, triggering a delayed break in the vortical structures in the wake region as the flow evolves toward its steady state.

Actuators emerge from the center of the lower channel wall. Measured in terms of the radius of the symmetric actuator (σ), the distance from the actuator centerline to the edge of each damping zone is 8.06. As an actuator rises, the intensifying structures that surround it stretch vertically into the mean flow, eventually extending into the damping region where they are artificially dissipated. To determine whether this downstream damping alters the nature of the structures in the immediate vicinity of the actuator, tests have been performed with and without damping.

Although the latter case is tantamount to a simulation of flow over an infinite array of actuators, it does give an indication of the downstream extent of the intensified structures before the point in time at which shedding occurs. An aspect of the flow dynamics beyond the scope of this investigation, the histories of these shed vortices may, perhaps, be better represented in a Lagrangian (rather than an Eulerian) frame of reference.

Section III contains descriptions of the simulations of various flows over various actuators. In all but one of the tests a common actuator speed is specified, which is of the same order of magnitude as the local flow velocity. As a separate test the speed is reduced

Received Aug. 30, 1995; revision received Jan. 11, 1996; accepted for publication Jan. 12, 1996.

*Engineering Consultant, Department of Mechanical and Aerospace Engineering. Member AIAA.

†Professor, Department of Mechanical and Aerospace Engineering. Member AIAA.

by a factor of 2 to determine the relation between this parameter and the time scale of the transient. Particular attention is paid to the streamwise vorticity as it is this component of the actuator-induced disturbance that will, in future work, be used to control the structures close to the wall during the bursting event in a turbulent wall layer.

II. Numerical Method

The domain consists of a channel with a flat top wall and a bottom wall that may be perturbed in time from its initial, flat configuration. In Euclidian space, the streamwise, wall-normal, and spanwise directions are denoted as x_1, x_2, and x_3, respectively. The top wall is located at $x_2 = +L_0$, the bottom wall at $x_2 = h - L_0$; L_0 is the channel half-height, and $h(x_1, x_3, t)$ denotes the wall perturbation.

Through a time-dependent, three-dimensional curvilinear coordinate transformation[8,10,11] the general domain is mapped to one that permits spectral representation of the solution[12,13] and preserves exact boundary conditions. Beginning with the Navier–Stokes equation in general tensor form, application of a metric operator effects the transformation. The primitive variables, velocity $\boldsymbol{u}$ and modified pressure p, may then be represented pseudospectrally: Fourier in the stream- and spanwise directions, Chebyshev wall normal.

The equation to be solved (nondimensionalized and in rotational form) is

$$\frac{\partial u_i}{\partial t} = -\frac{\partial p}{\partial x_i} + \epsilon_{ijk} u_j \omega_k + \frac{1}{Re}\frac{\partial^2 u_i}{\partial x_j \partial x_j} - \Theta(x_1)\, u_i \qquad (1)$$

$$p \equiv \tilde{p} + \tfrac{1}{2} u_i u_i \qquad \omega_i \equiv \epsilon_{ijk}\frac{\partial u_k}{\partial x_j}$$

The alternative tensor ϵ_{ijk} is $+1$ when i, j, k are in cylinder order, -1 when i, j, k are in anticyclic order, and 0 if any of the i, j, k are equal. The last term on the right-hand side of Eq. (1) damps actuator-induced disturbances leaving (and re-entering) the computational box:

$$\Theta(x_1) = \frac{1}{2\Delta t}\left\{\exp\left[-\left(\frac{x_1 - 0}{\xi}\right)^2\right] + \exp\left[-\left(\frac{x_1 - L_1}{\xi}\right)^2\right]\right\} \qquad (2)$$

where Δt is the discrete time step size. The minimum length of each damping zone is limited by numerical stability constraints. With the given box dimensions (Table 1) the fringe zones consume approximately 8% of the computational domain ($\xi = 0.12$).

The Reynolds number (Re) is based on mean streamwise velocity at midchannel (U_0) and on the channel half-height (L_0):

$$Re = (U_0 L_0)/\nu \qquad (3)$$

Units of velocity, length, and time are normalized then by U_0, L_0, and L_0/U_0, respectively. A local Reynolds number may be defined, based on the height of the obstacle (ε_*) and the local velocity (the mean velocity that would exist through the height interval in the absence of the obstacle):

$$Re_l = (U_l \varepsilon_*)/\nu \qquad (4)$$

The initial field is parabolic and so the local velocity is

$$U_l = \frac{U_0}{\varepsilon_*}\int_{-1}^{\varepsilon_* - 1}\left(1 - x_2^2\right) dx_2 \approx 0.12 U_0 \qquad (5)$$

Viscosity is constant, and the flow is solenoidal (incompressible):

$$\frac{\partial u_i}{\partial x_i} = 0 \qquad (6)$$

Modified pressure is defined as a scalar function that, when substituted into Eq. (1), satisfies Eq. (6) everywhere in the domain:

$$\frac{\partial^2 p}{\partial x_i \partial x_i} = \epsilon_{ijk}\frac{\partial}{\partial x_i}\left(u_j \omega_k\right) - u_i \frac{\partial \Theta}{\partial x_i} \qquad (7)$$

Flow is sustained (viscous effects overcome) through the inclusion of a mean streamwise pressure gradient that maintains a constant mass flux:

$$\int_{h-1}^{1}\left\langle\frac{\partial u_1}{\partial t}\right\rangle_{k_{1,3}=0} dx_2 = 0 \qquad (8)$$

where $\langle\cdot\rangle$ denotes Fourier decomposition and $k_{1,3} = 0$ corresponds to the mean value in a plane parallel to the walls. In the case of parabolic flow between two flat walls the gradient is $\langle \partial p/\partial x_1\rangle_{k_{1,3}=0} = -2/Re$.

In general, displacement of the lower wall constitutes a change in the control volume. With periodic conditions in the stream- and spanwise directions (no net mass flux), a solenoidal condition becomes irreconcilable. The problem is circumvented by specifying that the average wall perturbation is zero. This requirement is met by lowering the wall that surrounds the actuator. Because the actuator volume is a small fraction of the total, the final perturbation of the surrounding wall (from its original position) is two orders of magnitude less than the final height of the actuator (0.001 vs 0.120). For this same reason the downward velocity of the surrounding wall is two orders of magnitude less than the upward velocity of the actuator itself. With zero average wall perturbation, exact boundary conditions for velocity are

$$u_1|_{x_2=\pm 1} = 0 \qquad u_2|_{x_2=+1} = 0$$
$$u_3|_{x_2=\pm 1} = 0 \qquad u_2|_{x_2=-1} = \frac{\partial h}{\partial t} \qquad (9)$$

Boundary conditions for pressure are determined indirectly from the solenoidal condition via an influence matrix technique.[14] Velocity in the evolution equation is advanced in time by means of a three-step Runge–Kutta method.[15] In the limit as $Re \to \infty$, the solution error attributable to temporal discretization approaches $(\Delta t)^4$. At the chosen Reynolds numbers the error falls between $(\Delta t)^3$ and $(\Delta t)^4$. In a variable mode the time step size finds its maximum based on a numerical stability condition (the conventionally defined Courant–Friedrichs–Lewy number) and is of order 10^{-2}.

With respect to spatial discretization the solution of flow in a canonical channel (zero wall perturbation) is spectrally accurate.

Table 1 Parameters whose values are common in all test cases

Wall parameters	Time parameters	Box dimensions	Resolution
$\epsilon_* = 0.12$	$\Delta t \approx 0.0165$	$L_1 = \pi$	$N_1 = 80$
$\sigma = 0.18$	$T \approx 19$	$L_2 = 2$	$N_2 = 65$
		$L_3 = \pi/2$	$N_3 = 32$

Table 2 Parameter values that distinguish the six test cases

	Case					
	1	2	3	4	5	6
Damping	Yes	No	Yes	Yes	Yes	Yes
$\mu(x_1 \le (\pi/2)$	1	1	1	2	1	1
$\mu(x_1 \le (\pi/2)$	1	1	2	1	1	1
Re	2×10^3	2×10^3	2×10^3	2×10^3	5×10^3	2×10^3
Re_l	2.88×10^1	2.88×10^1	2.88×10^1	2.88×10^1	7.2×10^1	2.88×10^1
ϵ_*	0.0487	0.0487	0.0487	0.0487	0.0487	0.0244
ϵ_c	0.0953	0.0953	0.0953	0.0953	0.0953	0.0472

The round-off error that is incurred by the fast Fourier transformation subroutines is a machine-dependent quantity and is approximately 10^{-13}. Because covariant differentiation generates variable coefficient terms in the equations for pressure and velocity, an iterative solution scheme is required in the case of a noncanonical channel (nonzero wall perturbation). As a cost savings measure the number of required iterations is curbed by specifying a convergence tolerance of 10^{-7}, a value that falls between $(\Delta t)^3$ and $(\Delta t)^4$.

III. Analyses of the Flows

This section contains descriptions of six simulations of flow over an emerging obstacle. Parameters that distinguish the six test cases are Reynolds number, actuator shape μ and speed $\dot{\varepsilon}$, and inclusion (or omission) of damping at the inlet and outlet of the computational box. The values of these parameters are listed in Table 2. The actuators, whose centerlines are located in the middle of the lower wall, are defined by the following Gaussian function:

$$h(x_1, x_3) = \varepsilon(t) \exp\left\{-\sigma^{-2}\left[\left(x_1 - x_1^0/\mu\right)^2 + \left(x_3 - x_3^0\right)^2\right]\right\} \qquad x_1^0 = \pi/2; \qquad x_3^0 = \pi/4 \tag{10}$$

By varying the parameter μ three actuator shapes are obtained (see Fig. 1). The height ε is time dependent; the standard deviation σ is not, so that the obstacles rise uniformly as opposed to ballooning out. The term $\dot{\varepsilon}_*$ is the maximum actuator speed, $\ddot{\varepsilon}_c$ the set acceleration (deceleration).

Time histories of the flows consist of nine snapshots ($N = 1, 9$). At $N = 1$ all actuators are at approximately 75% of their maximum heights and are rising at constant speeds $\dot{\varepsilon}_*$. At $N = 2$ the actuators have just reached their target heights and are stationary. At $N = 9$ transients associated with the motions of the actuators have dissipated to below 10% of their peak values and the flows are approaching their final, steady states.

Case 1 is the simulation of lower Reynolds number flow over a symmetric actuator, rising at the higher speed. Damping zones are included. Presented first, this simulation provides a representative picture of the transient and constitutes a benchmark against which the other cases may be compared. The detailed description of case 1 will be followed by a dicussion of the differences between it and the other simulations.

Figure 2 provides a qualitative view of the flow dynamics: isosurfaces of streamwise vorticity. Note that units of time are L_0/U_0. As the actuator rises ($T = 2.098$), vertical vortex tubes extend from just above it to a point outside the view box. This matches the distribution of wall-normal velocity, which has a peak at some distance above the

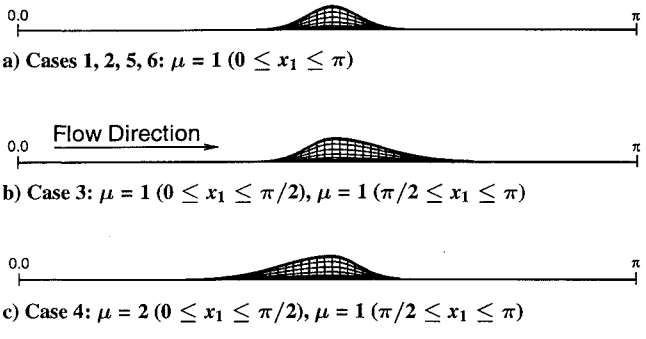

Fig. 1 Profiles of the actuators of Sec. III. Refer to Eq. (10) for a definition of the parameter μ.

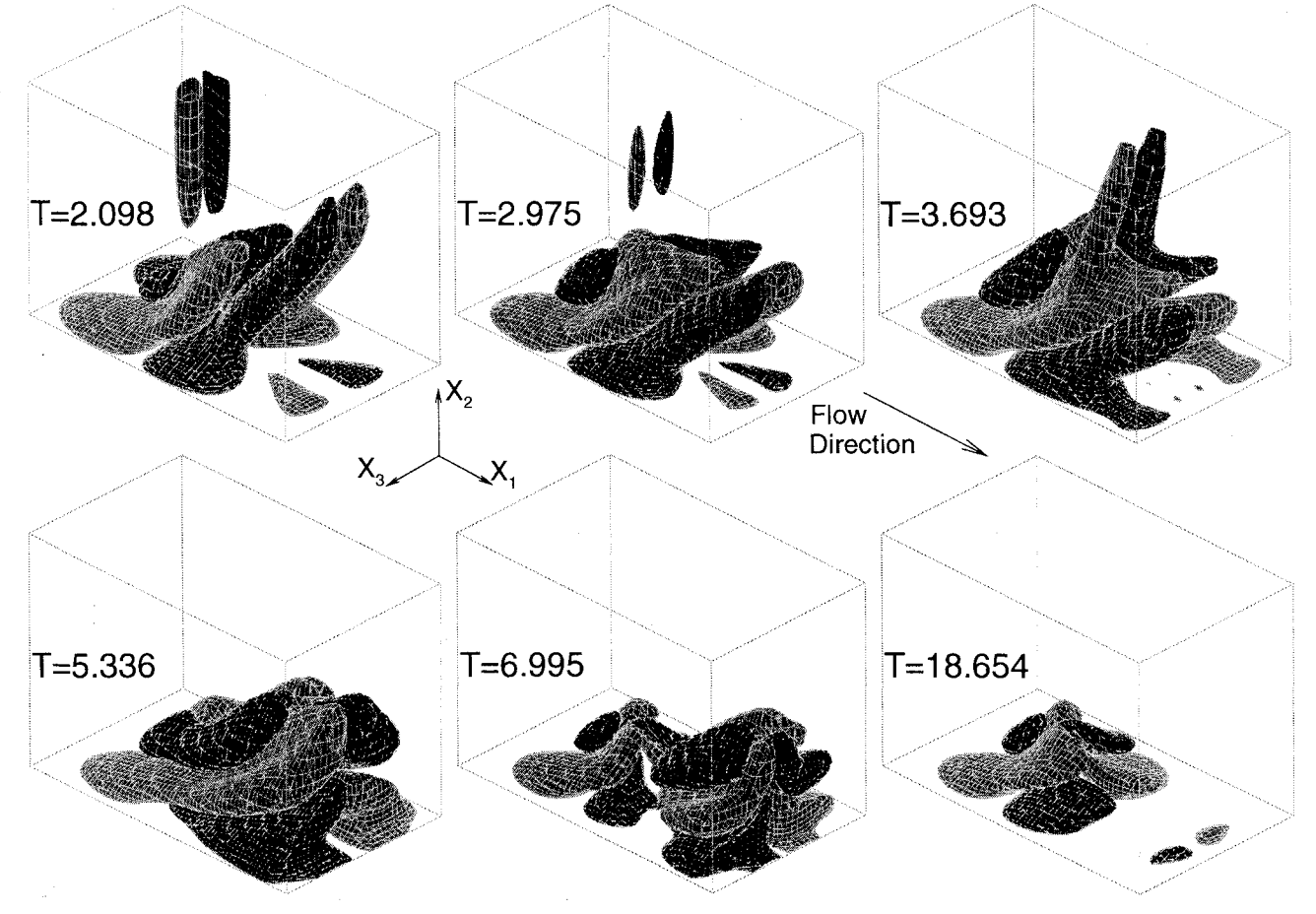

Fig. 2 Isosurfaces of streamwise vorticity (black negative valued, grey positive valued). Absolute values on and inside the surfaces are greater than 0.1. Each structure, lying directly on top of the actuator, is actually very close to the wall and so has been stretched by a factor of 3 in the wall-normal direction (for viewing purposes). The view box is only a fraction of the computational domain, extending from $x_2 = -1.000$ (the lower wall) to -0.428 in the wall-normal direction and from $x_1 = 0.628$ to the outlet in the streamwise direction. All structures are spanwise symmetric.

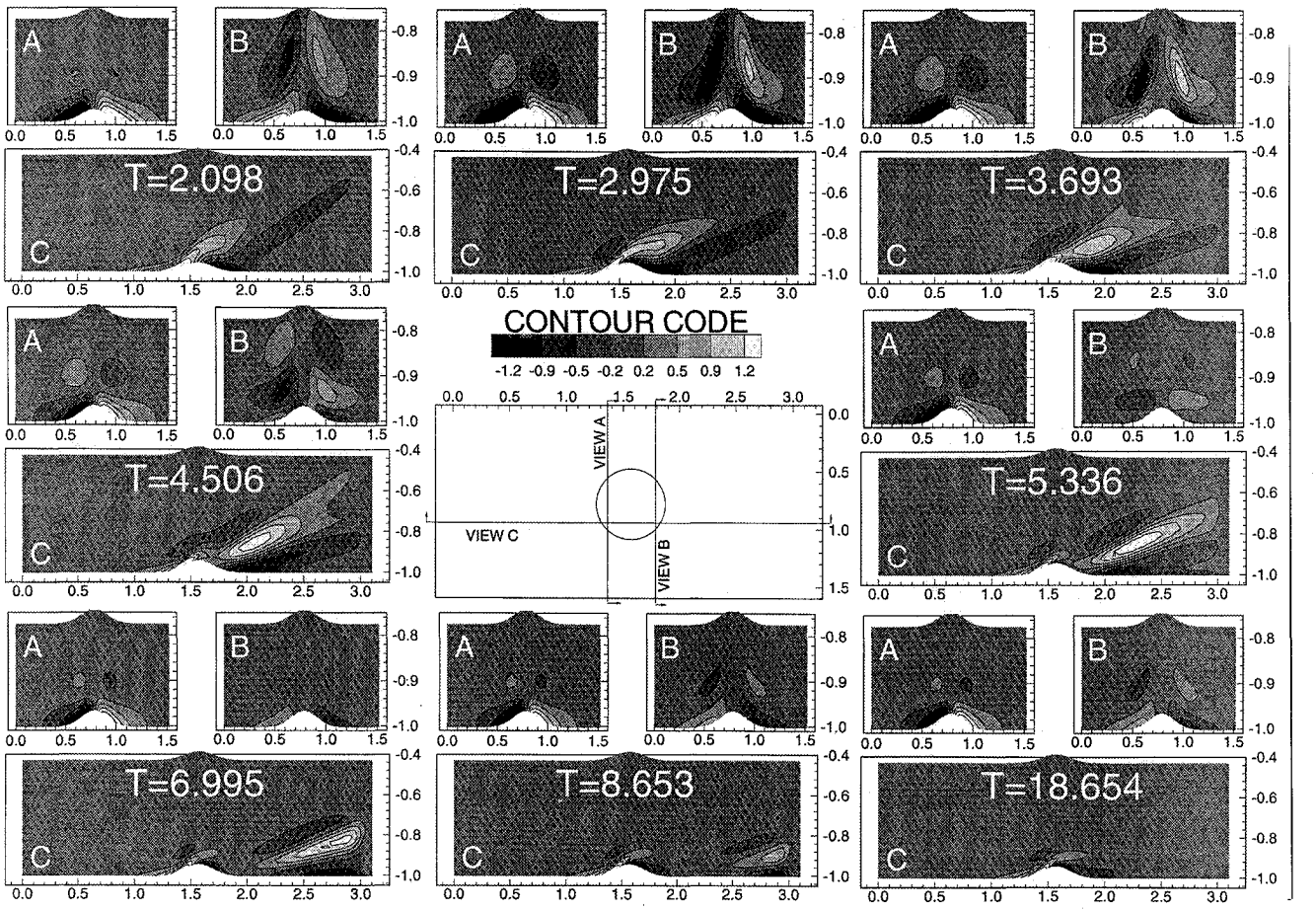

Fig. 3 Time history for case 1: contour plots of streamwise vorticity; A and B are front views up- and downstream of the actuator (at $x_1 = 1.374$ and 1.767, respectively), and C is a side view covering the length of the box (at $x_3 = 0.933$). The top of the actuator is located at $x_2 = -0.88$.

rising actuator. The actuator has decelerated to rest at $T = 2.975$ and the main structures overhead, which were being lifted by its upward motion, assume a more horizontal attitude and begin to fold onto one another. The vertical tubes dissipate, then regain strength by collapsing into and combining with the main structures. At $T = 5.336$ the folding caused by convection is complete and by $T = 6.995$ the structures have broken in two. The stronger downstream half is convected into the damping zone, leaving its weaker twin, which constitutes the final picture.

Streamwise vorticity is generated at the boundary from two sources: pressure gradients tangent to the wall and boundary layer (spanwise) vorticity that has been turned inertially.[16] A relation for the flux of vorticity may be obtained from the Navier–Stokes equation by rewriting the viscous term:

$$\frac{1}{Re}\frac{\partial^2 u_i}{\partial x_j \partial x_j} = \frac{1}{Re}\left[\frac{\partial}{\partial x_j}\left(\frac{\partial u_i}{\partial x_j} - \frac{\partial u_j}{\partial x_i}\right) + \frac{\partial}{\partial x_i}\left(\frac{\partial u_j}{\partial x_j}\right)\right] \tag{11}$$

From the solenoidal condition the second term on the right side is zero. The first term contains the rotation tensor, defined as

$$r_{ij} \equiv \frac{1}{2}\left(\frac{\partial u_i}{\partial x_j} - \frac{\partial u_j}{\partial x_i}\right) = -\frac{1}{2}\epsilon_{ijk}\omega_k \tag{12}$$

Substitution into the Navier–Stokes equation yields

$$\frac{\partial u_i}{\partial t} = -\frac{\partial p}{\partial x_i} + \epsilon_{ijk}u_j\omega_k - \frac{1}{Re}\epsilon_{ijk}\frac{\partial \omega_k}{\partial x_j} \tag{13}$$

At the lower wall, only the wall-normal component of velocity is nonzero and so the wall-normal flux of streamwise vorticity is

$$\frac{1}{Re}\frac{\partial \omega_1}{\partial x_2}\bigg|_{\text{wall}} = \left[-\frac{\partial p}{\partial x_3} + u_2\omega_1\right]_{\text{wall}} \tag{14}$$

The spanwise pressure gradient is primarily an inviscid effect, diverting flow around the obstacle upstream and back in behind it downstream. The other source of streamwise vorticity is inertially turned boundary-layer vorticity:

$$\omega_3 = \frac{\partial u_2}{\partial x_1} - \frac{\partial u_1}{\partial x_2} \tag{15}$$

From the curl of the Navier–Stokes equation one obtains a relation for the material derivative of vorticity:

$$\frac{\mathrm{D}\omega_i}{\mathrm{D}t} = \omega_j s_{ij} + \frac{1}{Re}\frac{\partial^2 \omega_i}{\partial x_j \partial x_j}$$
$$s_{ij} \equiv \frac{1}{2}\left(\frac{\partial u_i}{\partial x_j} + \frac{\partial u_j}{\partial x_i}\right) \tag{16}$$

The first term on the right-hand side of Eq. (16) represents inertial processing: the strain rate acting upon pre-existing vorticity.[17] Absent the actuator, the vorticity associated with a parabolic flow profile is simply $\omega_3 = \partial u_1/\partial x_2 = -2x_2$. Labeling this the order one vorticity, all of the rest is of order ε (where ε is the actuator height). So the primary contribution to the streamwise component is

$$\frac{\mathrm{D}\omega_1}{\mathrm{D}t} \sim \frac{\omega_3}{2}\left(\frac{\partial u_1}{\partial x_3} + \frac{\partial u_3}{\partial x_1}\right) \tag{17}$$

Figure 3 provides a quantitative picture of the evolution of streamwise vorticity. The weakest pair of vortices, farthest from the wall and upstream (views A), has a central downwash. This is inertially turned boundary-layer vorticity, which receives an additive contribution from the boundary velocity through the first term on the right side of Eq. (15). The inertial processing takes time as evidenced in the evolution of this pair: it is born as the actuator is rising ($T = 2.098$) but does not attain its peak intensity until 0.718

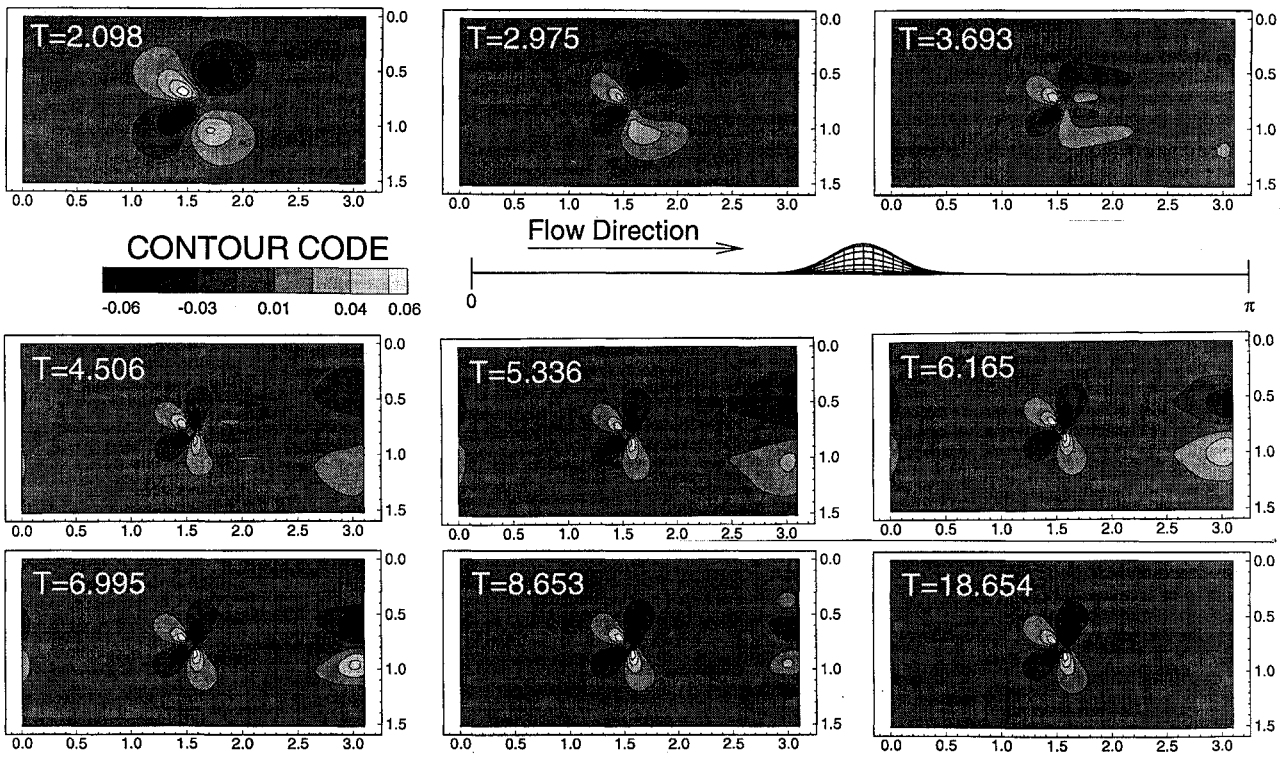

Fig. 4 Time history for case 1: contour plots of the spanwise pressure gradient at the lower wall.

time units after the actuator has stopped. Subsequently, diffusive effects slowly diminish the pair's intensity.

Close to the wall are a pair with central upwash (upstream of the actuator) and a pair with central downwash (downstream). These pairs, whose source is the spanwise pressure gradient, indicate diversion of flow around the obstacle. From view C in Fig. 3, the upstream pair extends downstream of the actuator centerline, showing up as the topmost stacked pair in view B. While the actuator is rising ($T = 2.098$), all of the structures are both convected and lifted, resulting in attitudes of 0.4, approximately equivalent to the ratio of actuator speed to local flow velocity ($\dot{\varepsilon}_*/U_l = 0.406$).

Following deceleration, the attitudes of the two upstream pairs remain unchanged on the upstream side as the fluid is lifted over the actuator. Downstream, the attitudes decrease as the fluid is forced down the backside (absent any boundary velocity). The resulting kink in the structures, manifestation of a growing instability, leads to their breaking in half at $T = 5.336$. Comparison of the final field (at $T = 18.654$) with snapshots before the break up (at $T = 2.975$ for instance) discloses a common qualitative picture. The differences lie in the strengths of the vortex pairs, the steady solution consisting of less intense structures.

At all times peak values of the lower structures are located at the wall. The maxima at the wall at $T = 3.693$ are two (upstream) and four (downstream) times higher than the maxima at $T = 18.654$. Boundary velocity contributes to both sources of streamwise vorticity: to the boundary-layer vorticity through the first term on the right-hand side of Eq. (15) and to the pressure gradient-induced vorticity through the second term on the right-hand side of Eq. (14).

Figure 4 is a time history of the spanwise pressure gradient at the lower wall. The pair of structures just upstream of the actuator maintains a fixed position throughout the course of the simulation, having intensified and spread as the actuator rose ($T = 2.098$). As the actuator decelerates to rest at $T = 2.975$, the intensification and the spreading are reversed almost instantaneously. The two structures downstream of the actuator are separated by a gap of zero gradient. By $T = 2.975$ this gap has widened, and at $T = 3.693$ a new pair of structures forms directly behind the actuator.

The pressure gradient associated with this pair generates a region of counter-rotating flow and signals the onset of vortex shedding. By $T = 5.336$, this smaller pair has disappeared and the dominant pair downstream, which indicates convergence of flow around the backside of the actuator, possesses its final shape, position, and level of intensity. Although the upstream pair is considerably stronger than the pair downstream at $T = 2.098$, indicating stronger divergence around the actuator than convergence behind it, the reverse is true at $T = 18.654$. The structures that appear near the outlet of the computational box at $T = 3.693$, and that persist through $T = 8.653$, are artifacts of the damping zones.

Figure 5 is a time history of the surface stress pattern at the lower wall. At $T = 2.098$ and 2.975 a well-defined separation zone exists behind the actuator, enhanced by the vertical velocity of the boundary. At $T = 3.693$, the small region of counter-rotating flow begins to form downstream and the region persists through $T = 6.165$. Having passed through this inflectional cycle, the flow around the actuator arrives at its final configuration at $T = 6.995$, which consists of attached flow upstream with downstream separation.

Figure 6 contains time histories of centerplane streamlines (upper panels) and contours of the streamwise strain rate at the wall (lower panels). Streamlines emanate from the actuator at $T = 2.098$, giving rise to a stagnation zone on its upstream side. This zone, exclusively the result of boundary velocity, disappears as the actuator decelerates. Snapshots of the centerplane streamlines illustrate the inflectional cycle of the flow in the wake region. As a baseline for values in the contour plot, the strain rate corresponding to a parabolic profile (absent the actuator) is $+2(U_0/L_0)$. The region of high strain, located atop the actuator, grows and intensifies in time, reaching a maximum value of approximately $+12.0(U_0/L_0)$. The minimum value in the wake region is $-2.0(U_0/L_0)$.

Comparison of cases 1 and 2 (with and without damping) confirms that the flow dynamics adjacent to the actuator, vortex shedding and the inflectional cycle, are unaffected by the damping zones. Just before the vortex shedding event ($T = 4.506$ in Fig. 3, view C), the vortical structures closest to the wall and downstream of the case 1 actuator extend to $x_1 = 3.0$, the edge of the downstream damping zone. At this point in time during the case 2 simulation,

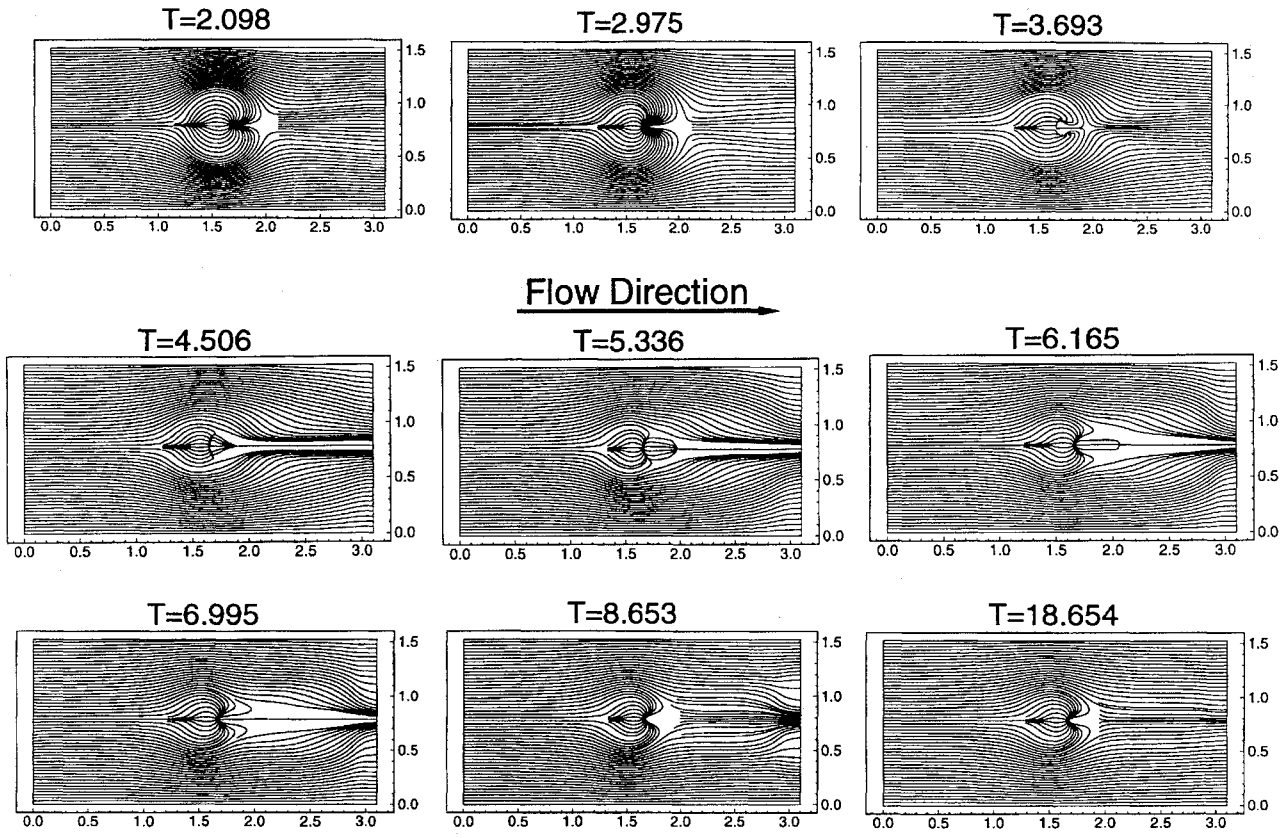

Fig. 5 Time history for case 1: surface stress patterns at the lower wall. Streamlines are constructed from the stream- and spanwise components of wall shear stress and indicate the direction of flow close to the wall. Partial streamlines have been inserted, particularly downstream of the stagnation point.

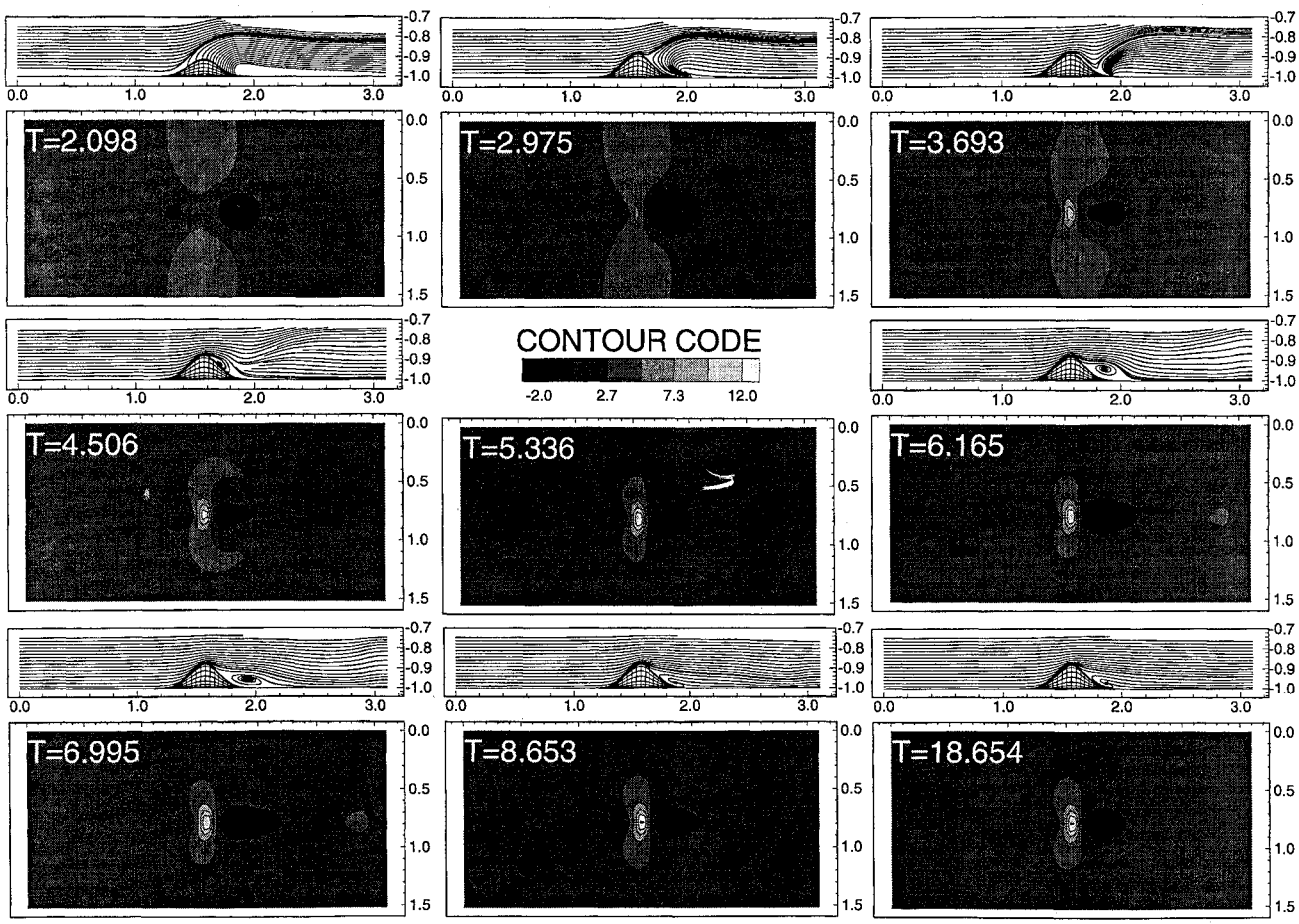

Fig. 6 Time history for case 1: centerplane streamlines (upper panels) and contour plots of the streamwise strain rate at the wall (lower panels). Units of the strain rate are U_0/L_0.

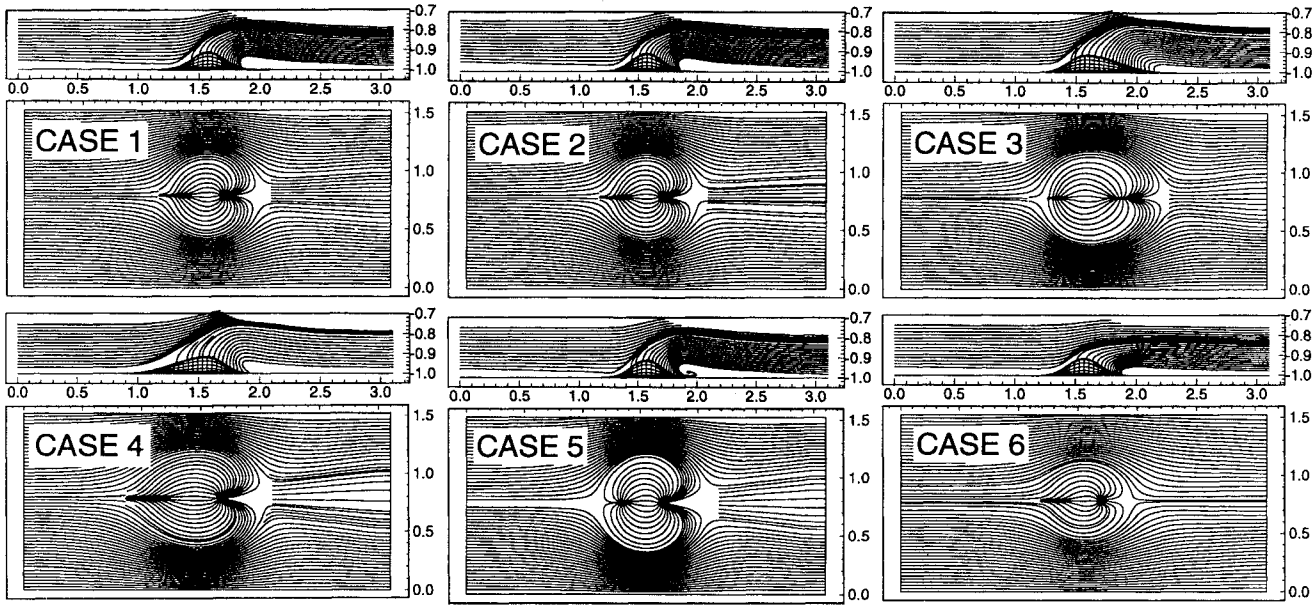

Fig. 7 Centerplane streamlines (upper panels) and surface stress patterns (lower panels) for all six cases at $N = 1$ (each actuator is rising at a speed of $\dot{\varepsilon}_*$ and is at 75% of its target height). Partial streamlines have been inserted, particularly downstream of the stagnation point.

the same structures have been convected through the outlet of the computational box and back into the inlet, extending the full length of the domain. Because they have been lifted by the rising obstacle, the extended vortices are well above the wall and do not interact with the structures surrounding the actuator.

The skew-symmetric actuators of cases 3 and 4 and the symmetric actuators at higher Reynolds number (case 5) and at half-speed (case 6) induce transients very similar to that which has been described for case 1. Regarding differences in the final, steady solutions, the actuator with a gently sloping frontside (case 4) produces no measurable, inertially turned boundary-layer vorticity on its upstream side, and the surface stress pattern for case 3 indicates attached flow downstream of the actuator with a gently sloping backside. The convection of vortical structures is strongest at the higher Reynolds number (case 5), and the steady-state structures closest to the wall are squatter and more intense than those of case 1. Finally, the higher Reynolds number flow alone produces a (small) downwash pair of vortices directly in front of the actuator.

Because of the amount of space they consume, complete time histories for cases 2–6 have been omitted. However, they do depict some unique features worth mentioning. Figure 7 contains plots of centerplane streamlines (upper panels) and surface stress patterns (lower panels) at $N = 1$. In cases 1 and 2, small stagnation zones upstream of the actuators appear as they rise. The higher Reynolds number flow of case 5 is fully detached both up- and downstream at $N = 1$. Interestingly, flow upstream of the actuator with a gently sloping backside (case 3) becomes slightly detached as it rises.

Even though the final flow of the case 3 actuator is fully attached, antecedent transients occur that are common in all cases. A broad separation region prevails downstream even after the actuator has stopped rising. At $T = 3.726$ the flow reattaches, separates again at $T = 5.290$, and finally reattaches for good at $T = 8.666$. This cyclic behavior illuminates the nature of the transient. Following a fairly rapid deceleration, adjustment of the flow is overcorrective as it begins converging downward on the backside of the actuator.

Regarding the time scale of the transient, vortex shedding occurs approximately 0.8 time unit (one snapshot) later with the skew-symmetric shapes than with the symmetric actuators of cases 1, 2, and 5. The vertical velocity of the boundary adds to the natural upward motion of the fluid as it rises to avoid the obstacle on the upstream side and subtracts from the natural downward motion as it converges on the backside.

Upon turning off this boundary velocity, the mean flow quickly begins to converge downward on the backside, and this reversal of direction produces, through inertial processing, a kink in the preexisting vortical structures. The kink is less pronounced in case 3 because the gently sloping backside does not promote the same level of downward, converging flow. The kink is less pronounced in case 4 because the gently sloping frontside induces less lifting upstream. Consequently, the transients take slightly longer to play themselves out.

Reynolds number has a negligible effect on the time scale of the transient. The critical parameters are $\dot{\varepsilon}_*$ and $\ddot{\varepsilon}_c$ that, together with ε_*, determine the time of rise of an actuator:

$$T_* = (\varepsilon_*/\dot{\varepsilon}_*) + (\dot{\varepsilon}_*/\ddot{\varepsilon}_c) \tag{18}$$

The rising times T_* for the faster and slower moving actuators (cases 1 and 6, respectively) are 2.975 and 5.435. The vortical structures begin to break at approximately $T = 5.226$ (case 1) and 7.868 (case 6). Normalized by their corresponding values of T_*, these times become 1.757 and 1.448. Relative error in the normalized times is 17.59%, indicating that T_* is a fairly good approximation of the time scale of the transient.

IV. Conclusion

The dynamics of laminar flow over a rapidly emerging obstacle consist of vortical structures identical to those found in flow over a stationary obstacle, intensified and stretched by the upward velocity of the boundary. During the rise of an actuator the structures intensify by a factor of 2 and extend to three times their steady-state lengths, assuming more vertical attitudes as they are lifted by the moving boundary. Following deceleration the amplification leads to a transient, triggering a break in the vortical structures and temporary counter-rotation downstream of the actuator as the flow evolves toward its steady state.

Just before the point at which they break, the vortical structures in the case 2 simulation (no damping) have stretched to more than six times their steady-state lengths. Boundary velocity intensifies the streamwise vorticity directly through terms in the equations for inertially turned boundary-layer vorticity and for the pressure gradient-induced vorticity, so that the degree of intensification (and the extent of stretching) is a direct function of actuator speed.

A range of parameter values (actuator shape and speed, Reynolds numbers) have allowed for analyses covering a range of flows. Distinguishing characteristics include temporary upstream stagnation zones (in cases 1 and 2), temporary upstream separation (in case 5), and attached flow downstream in the steady state (case 3). Shape and Reynolds number determine the pattern and strengths of steady-state vortical structures; actuator speed determines the

degree of short-term amplification. Common in all test cases is the transient.

Because the chosen algorithm is pseudospectral, requiring periodic boundary conditions, damping zones were included to simulate flow, undisturbed on the approach, over a solitary actuator. Comparison of cases 1 and 2 (with and without damping) indicates that the zones have no effect on dynamics adjacent to the actuator: salient features of the transient, the vortex shedding event and inflectional cycle, are identical. Exclusion of the damping zones reveals the full extent of the amplified structures before the point at which they break.

Within the range of chosen values, Reynolds number has a negligible effect upon the time scale of the transient. Through differences in the inertial processing of vorticity, actuator shape has a modest effect. The comparative test using two different speeds and accelerations indicates that the rising time of an actuator figures most prominently in determining the duration of the transient.

The laminar flow simulations provide baseline data that will be used in an investigation of active control in the wall layer of a minimal flow unit.[18] Defined as the smallest computational box that will sustain a turbulent field, the minimal unit contains one pair of coherent structures, a high- and a low-speed streak and provides a manageable setting that, because of the time-dependent wall geometry, would be prohibitively expensive to simulate otherwise. The control strategy will consist of using vortical structures (the updrafts and downdrafts) generated by an actuator to redistribute momentum close to the wall, thereby controlling the skin-friction drag.

Acknowledgments

The research was supported by Contract F49620-92-J-0287 jointly funded by the U.S. Air Force Office of Scientific Research (Control and Aerospace Programs) and the U.S. Office of Naval Research. Computational resources were provided by the National Science Foundation Supercomputer Facility located at Cornell University. The authors thank Sidney Leibovich of Cornell University for his help in interpreting the results of the simulations.

References

[1]Choi, H., Moin, P., and Kim, J., "Active Turbulence Control for Drag Reduction in Wall-Bounded Flows," *Journal of Fluid Mechanics*, Vol. 262, March 1994, pp. 75–110.

[2]Coller, B. D., Holmes, P., and Lumley, J. L., "Interactions of Adjacent Bursts in the Wall Region," *Physics of Fluids*, Vol. 6, No. 2, 1994, pp. 954–961.

[3]Hunt, J. C. R., and Snyder, W. H., "Experiments on Stably and Neutrally Stratified Flow over a Model Three-Dimensional Hill," *Journal of Fluid Mechanics*, Vol. 96, Pt. 4, 1980, pp. 671–704.

[4]Jenkins, G. J., Mason, P. J., Moore, W. H., and Sykes, R. I., "Measurements of the Flow Structure Around Ailsa Craig, a Steep, Three-Dimensional Isolated Hill," *Quarterly Journal of the Royal Meteorological Society*, Vol. 107, No. 454, 1981, pp. 833–851.

[5]Duck, P. W., and Burggraf, O. R., "Spectral Solutions for Three-Dimensional Triple-Deck Flow over Surface Topography," *Journal of Fluid Mechanics*, Vol. 162, Jan. 1986, pp. 1–22.

[6]Mason, P. J., and Sykes, R. I., "Three-Dimensional Numerical Integrations of the Navier–Stokes Equations for Flow over Surface Mounted Obstacles," *Journal of Fluid Mechanics*, Vol. 91, Pt. 3, 1979, pp. 433–450.

[7]Mason, P. J., and Morton, B. R., "Trailing Vortices in the Wakes of Surface-Mounted Obstacles," *Journal of Fluid Mechanics*, Vol. 175, Feb. 1987, pp. 247–293.

[8]Carlson, H. A., Berkooz, G., and Lumley, J. L., "Direct Numerical Simulation of Flow in a Channel with Complex, Time-Dependent Wall Geometries: A Pseudospectral Method," *Journal of Computational Physics*, Vol. 121, No. 1, 1995, pp. 155–175.

[9]Bertolotti, F. P., Herbert, T., and Spalart, P. R., "Linear and Nonlinear Stability of the Blasius Boundary Layer," *Journal of Fluid Mechanics*, Vol. 242, Sept. 1992, pp. 441–474.

[10]Voke, P. R., and Collins, M. W., "Forms of the Generalised Navier–Stokes Equations," *Journal of Engineering Mathematics*, Vol. 18, No. 3, 1984, pp. 219–233.

[11]Gal-Chen, T., and Somerville, R. C. J., "On the Use of Co-Ordinate Transformation for the Solution of the Navier–Stokes Equations," *Journal of Computational Physics*, Vol. 17, No. 2, 1975, pp. 209–228.

[12]Canuto, C., Hussaini, M. Y., Quarteroni, A., and Zang, T. A., *Spectral Methods in Fluid Dynamics*, Springer–Verlag, Berlin, 1988.

[13]Gottlieb, D., Hussaini, M. Y., and Orszag, S. A., "Theory and Applications of Spectral Methods," *Spectral Methods for Partial Differential Equations*, edited by R. G. Voigt, D. Gottlieb, and M. Y. Hussaini, Society for Industrial and Applied Mathematics, Philadelphia, PA, 1984, pp. 1–54.

[14]Kleiser, L., and Schumann, U., "Treatment of Incompressibility and Boundary Conditions in 3-D Numerical Spectral Simulations of Plane Channel Flows," *Proceedings from the 3rd GAMM Conference on Numerical Methods in Fluid Mechanics*, Vieweg, Braunschweig, Germany, 1980, pp. 165–173.

[15]Spalart, P. R., Moser, R. D., and Rogers, M. M., "Spectral Methods for the Navier–Stokes Equations with One Infinite and Two Periodic Directions," *Journal of Computational Physics*, Vol. 96, No. 2, 1991, pp. 297–324.

[16]Rosenhead, L. (ed.), *Laminar Boundary Layers*, Clarendon, Oxford, England, UK, 1963, pp. 48–113.

[17]Tennekes, H., and Lumley, J. L., *A First Course in Turbulence*, MIT Press, Cambridge, MA, 1989, pp. 75–84.

[18]Jimenez, J., and Moin, P., "The Minimal Flow Unit in Near-Wall Turbulence," *Journal of Fluid Mechanics*, Vol. 225, April 1991, pp. 213–240.